Chapter 6

Prestack Time and Depth Migration

Prestack migration algorithms are relatively simple variants of the poststack methodologies. The primary difference lies not in the mathematical theory but in the way in which any given algorithm is structured and applied to recorded multi-fold data. The basic differences arise because the prestack method must handle non-coincident sources and receivers. This means that it must handle the traveltime issues and amplitude correction factors associated with the source and similar issues for each and every receiver.

To resolve this issue, it is normal to split the imaging problem into two independent pieces. One piece handles the traveltime and amplitude from the source to the image point, while the other handles the traveltime and amplitude from the image point to the receiver. When both pieces are based on the same modeling approach, the names of the prestack algorithms are frequently identical to those given to the poststack methods from which they arose. When the two pieces are based on technically different methods, the resulting algorithm is assigned a hybrid combination of the two names. Figure 4-1 details these methodologies and becomes the framework for the discussion on zero offset technologies.

Wavefield and Wave-Motion Hierarchies

In Chapter 8, we noted the possibility of recording elastic as well as acoustic data. Figure 6-1 shows a simplified diagram of the kinds of waves you might encounter in a typical seismic acquisition experiment.

Figure 6-1. Wavefield hierarchy

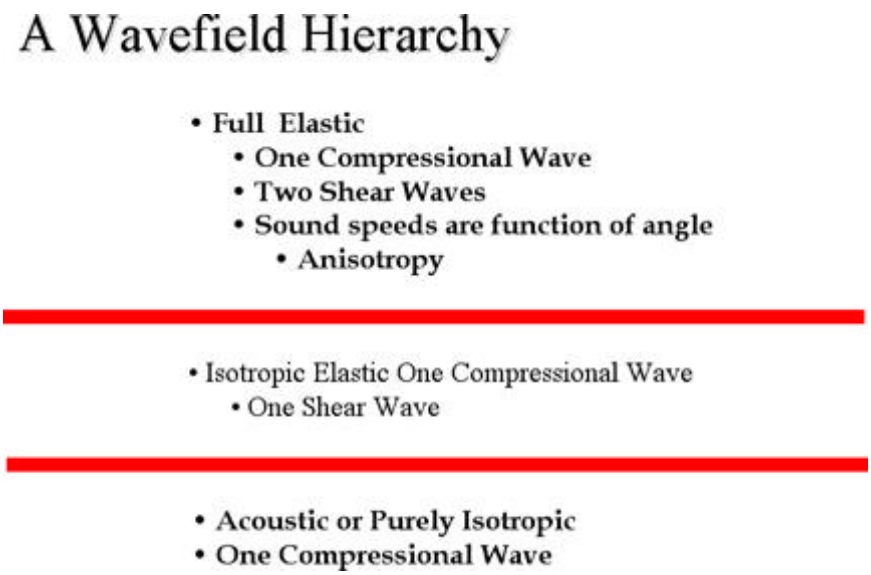

At the top of Figure 6-1, we see what is probably closest to what happens in the real earth. It is what we should record if we are serious about producing the best possible representation of the subsurface rocks. At the bottom, we see the kinds of waves that most of the migration algorithms of the recent past were designed to handle. This focus on the lowest rung of the ladder was dictated by the lack of sufficient computer power to consider imaging anything other than acoustic waves.

Between these two extremes, we see a wavefield middle ground that was once considered to define a sufficient data set for most, if not all, exploration goals. This has also proven to be false. While it is quite easy to construct middle-ground algorithms based on the technology we have discussed to this point, the possibility of stepping from the bottom rung to the top rung is rapidly making the middle rung obsolete. Moreover, what is important is that zero-offset methods have little or no chance of imaging the complex kinds of waves that occur in the earth. Effective imaging of compressional and shear waves that constantly convert from one to the other can only be contemplated through the use of prestack methods.

Wavefields in almost any medium radiate in all directions. The normal at any given subsurface location to the propagating wave front points in the direction of what we commonly think of as a ray. Since the propagation is normally not constrained with regard to direction, this normal is allowed to point in any direction consistent with the

sound speed of the medium. If the normal points upward, we say that this is an upward traveling wave. If it points downward, we call it a downward traveling wave. Clearly, such fields change directions at 45 degrees and become purely horizontal waves at 90 degrees. As we track any given normal or ray, we quickly observe that not only can it travel horizontally but it can also turn up and propagate upward.

Figure 6-2 shows the kind of wavefields we can model based purely on choice of algorithm. Choosing one of the algorithms defined in Figure 4-1 means that we inherently assume the propagation characteristics of that particular approach. Unless we happen to choose the algorithm that exactly fits the actual earth propagation, some part of the true wavefield will not be properly imaged. It should be clear that any assumption limiting wavefield directions cannot be correct: It cannot accurately handle amplitudes; it will likely produce artifacts; and it may not be able to image recorded events.

Figure 6-2. A wave-motion hierarchy.

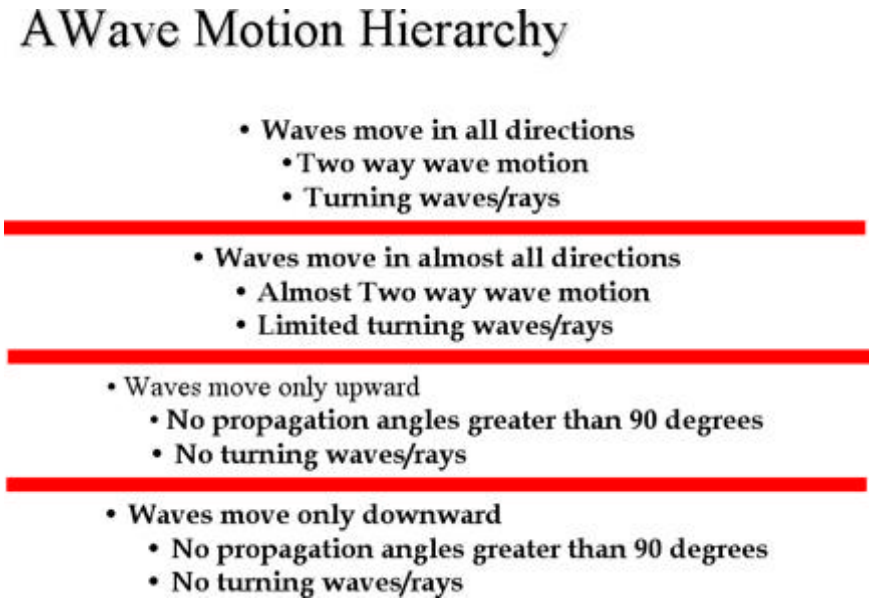

The only good news is that every algorithm in Figure 4-1 on page 134 is simply an approximation to the more accurate one at the top. Thus, given results from the bottom level, we should be able to step up to the next level, by simply running the more accurate approach.

Shot Profile Prestack Migration

Shot profile migration is a process by which each shot record is migrated separately and the result is summed into the final image volume. This process is sometimes also called *common-shot migration* or just *shot migration*.

Performing Shot Profile Migration

Shot-profile migration consists of three steps. In the first step, a synthetic shot is generated and propagated into the Earth. In the second step, receiver traces are reversed in time, used as sources in the modeling code, and then downward continued into the Earth. The third step forms an image at each depth or time slice through the application of an appropriate *imaging condition*.

This three-step approach is based on what is known as the *cross-correlation method* and was popularized by Jon Claerbout (1971, 1986). Figure 6-3 conceptualizes the basic ideas. The left hand side of this figure represents the forward propagation of the shot into the Earth, while the right hand side shows the backward propagation of the traces corresponding to this shot. In this figure, shot synthesis is generating a downward traveling wavefield, while the backward propagation of the receiver traces is generating what ultimately becomes an upward traveling wavefield.

Figure 6-3. Migration of common shot profiles

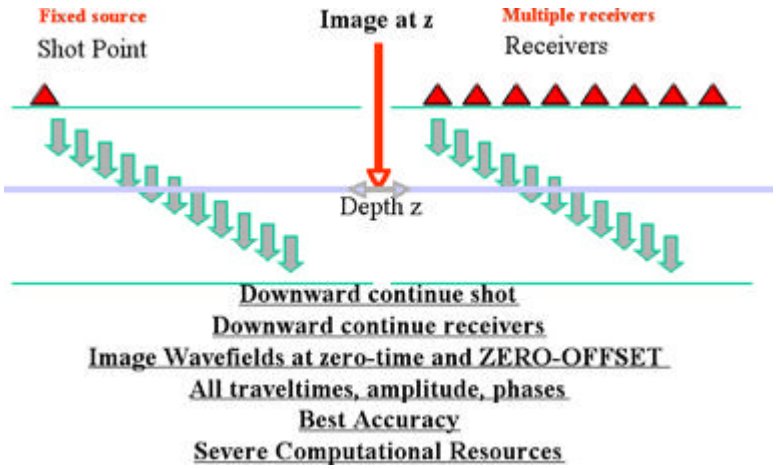

Note that we can choose virtually any pair of modeling algorithms for the basis of shot-profile migration. When a full two-way approach is used for both the shot and receiver steps, the result is a full two-way algorithm. When a one-way wave equation is used for both the shot synthesis and receiver back-propagation, the result is definitely a one-way method. Of course, it is possible to use two different modeling methods. We could use

a raytrace-based method for the shot synthesis and a full two-way back-propagation for the time-reversed receiver traces. Virtually any combination of the modeling algorithms discussed in Chapter 2 on page 7 is possible, so the number of prestack shot profile methods is quite large. We will avoid giving these hybrid methods names, but we will attach names to methods for which the shot synthesis and receiver back-propagation methods are algorithmically identical.

Understanding shot-profile migration is mainly dependent on comprehension of the third (imaging-condition) step of the shot-profile migration methodology since the modeling pieces are straight forward. To help understand the imaging condition, recognize that, as shown by the red dot in the movie corresponding to the image in Figure 6-4, each subsurface image point can be thought of as a seismic receiver that records signals from both the source and the receivers. The trace from the downward traveling source wavefield registers no arrivals until the first source amplitude arrives after τ_S seconds. This, of course, is the time it takes for energy from the source to ignite the virtual reflector at the image point.

Figure 6-4. A wavefield arriving at a subsurface image point (in red)

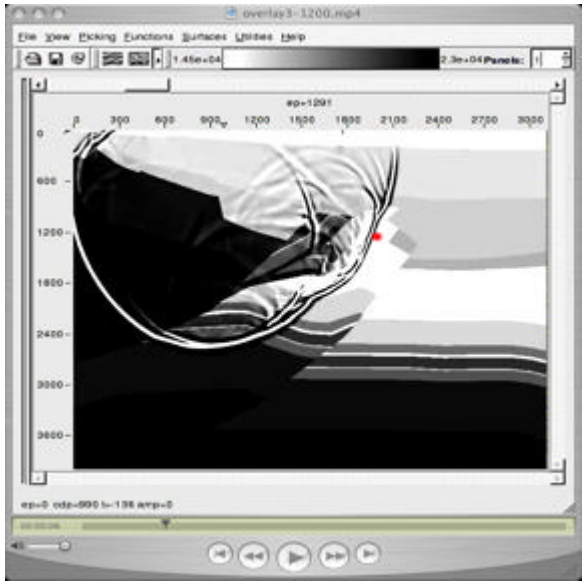

An example of such a trace showing two arrivals recorded from a source is shown in the top trace in Figure 6-5. An example of a second trace showing three arrivals from the backward propagated receivers is shown in the bottom trace. Because it was generated from time-reversed traces, amplitudes at the longest time are due to amplitudes recorded at the maximum recording time, τ_{max}. After backpropagating for $\tau_{max} - \tau_S$ seconds, the full wavefield that radiated out from the image point as it acted as a virtual source has arrived at the receiver located at the image point. At this time stamp, there are still τ_S seconds left to propagate, but none of these amplitudes will be recorded at the image point. Thus, both traces contain exactly two arrivals. Imaging is accomplished by summing all the amplitudes in a a point-by-point multiplication of the two traces and then adding the result to the image point location. This is exactly Jon Claerbout's cross-correlation imaging condition (1971, 1976) in graphic detail.

Figure 6-5. Downward (source) and Upward (receiver) arrivals at a subsurface image point

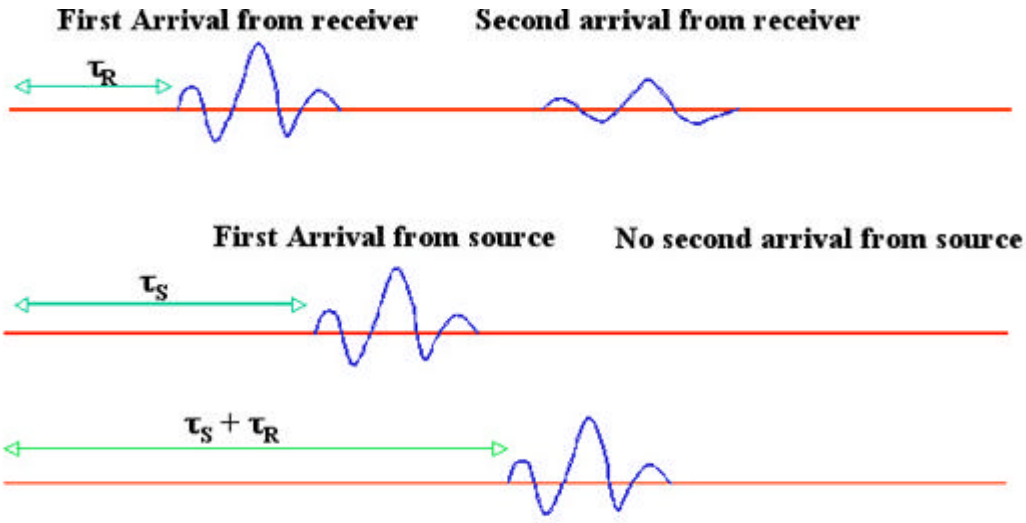

Figure 6-6 is a further attempt to clarify Claerbout's imaging condition. This figure shows a subsurface model with a single point reflector in red on the face and the time section indicated by the blue arc on the top. It contains three potential point reflectors indicated by two black dots and one red dot. The red dot is the only point reflector in the model.

Figure 6-6. Point reflector response with forward source and backward receiver wavefields at two subsurface locations.

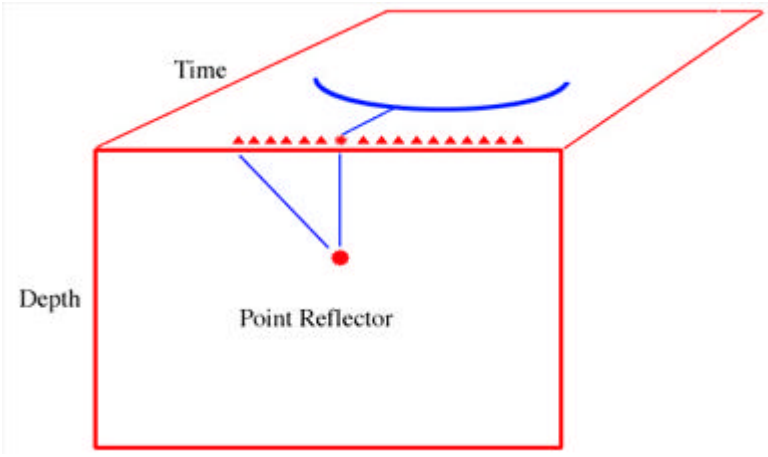

We see that events on the two recorded traces do not overlap at the upper black image point. Thus, applying the imaging condition produces zero amplitude and no reflectivity, as predicted, and no point reflector is detected. On the other hand, at the black dot that is near the red point reflector, the events on the two traces may be close enough to the red dot to produce a small amplitude, and as a result the point reflector begins to be detected. Claerbout's imaging condition is just the ticket for detecting the only point reflector in the model.

It may not be surprising that there was more than one arrival in each of the two traces at the image point. As indicated in the propagating wavefield in Figure 6-4(a), multiple paths from the source location to any subsurface image point is probably the norm in complex geology. In spite of that, it is important to recognize that there are several algorithms that make the surprising assumption that only one arrival is present at each subsurface location. We will see that single arrival methods, while useful, are very sensitive to the kinds of velocity variations seen in even relatively simple geologic settings.

As was the case on historical approaches in Chapter 3, migration was performed by hand on a shot-by-shot basis. In that case, the imaging was based on direct estimation of local dips coupled with a crude velocity guess. To emulate this process using our modeling methods, it was necessary account for the propagation from the source to the reflection point, and from the reflection-point to the receiver for each and every trace in our survey. This was accomplished by a forward shot propagation and a backward propagation using the recorded data reversed in time as sources. Clearly, both steps could employ exactly the same modeling code. The only real difference between the two is that one used synthetic source data while the other used the actual recorded data in reverse time order. Do not be discouraged if this does not seem simple or intuitive. In 1971, very few practicing geophysicists thought anything like this would ever be possible and many thought Claerbout's method would never be practical. They were wrong.

In precise mathematical terms, Claerbout's time-coincident imaging condition is mathematically represented by Equation 6-1, where $I(x,z)$ represents the seismic amplitude at the position (x,z) in space and depth, $S(t,x,z)$ is the downward traveling source wavefield, and $P(t,x,z)$ is the backward-propagating seismic-shot record.

(6-1) $$I(x,z) = S(t,x,z) \otimes P(t,x,z) \Rightarrow t = 0$$

In this case, $\otimes$ is interpreted to mean cross-correlation and $\Rightarrow t = 0$ means to evaluate at zero time for this depth. This process usually takes place in the frequency domain, so evaluation at time zero just means to sum over frequency. In this case, the formula is given by Equation 6-2.

(6-2) $$I(x,z) = \sum_{\omega} \overline{S(\omega,x,z)} P(\omega,x,z)$$

Refinements to this simple process abound. One of the simplest improvements is given by Equation 6-3.

(6-3) $$I(x,z) = \frac{\sum_{\omega} \overline{S(\omega,x,z)} P(\omega,x,z)}{\sum_{\omega} \overline{S(\omega,x,z)} S(\omega,x,z)}$$

This improvement in the frequency domain normalizes Equation 6-2 by the spectrum of the source wavefield. Because the source wavefield is what illuminated the subsurface in the first place, dividing by this value has the general affect of correcting for uneven illumination. It generally results in improved amplitude preservation, but should not be considered as the final word in amplitude preservation.

When the velocity field is exact, the imaging condition, as described by equations 6-1 and 6-3, produces sharp and accurate maps of subsurface reflectivity. When the velocity field is incorrect, many point reflectors may not be imaged or may be imaged very poorly.

It is quite natural to ask if there is some modification to the image condition that might make it possible to assess the accuracy of the velocity field or even to produce a method to estimate velocity corrections. One answer to this question is given by the non-zero offset imaging condition in Equation 6-4, and the other by the time shift zero offset condition in Equation 6-5.

(6-4) $$I(x,z,h) = S(t,x-h,z) \otimes P(t,x+h,z) \Rightarrow t = 0$$

(6-5) $$I(x,z,\tau) = S(t-\tau,x,z) \otimes P(t,x,z)$$

In Equation 6-4, h is a scalar with units of feet or meters at depth that measures where the two wavefields achieve maximum lateral correlation. It defines a range of subsurface

offsets that, in principle, offers the possibility for sensing and correcting for velocity errors. When the migration velocity is incorrect, the best image will appear at some positive or negative h. How far the wavefields are separated can be used to estimate a new velocity volume or field.

In Equation 6-5, τ is a scalar at depth with units of time that tells us how close the two wavefields are in time at depth. The scalar τ is not directly related to surface time; it is merely a value indicating the difference between forward source and backward receiver times. Instances where non-zero τ's produce the best image indicate inaccurate velocities, and the value of τ becomes useful in estimating a new velocity field.

It is worth noting that both of these approaches can be converted to methods that produce gathers parameterized by opening or reflection angle and azimuth in 3D. The mathematics are beyond the objectives of this book, but these migration angle gathers can be analyzed in much the same way that more traditional offset gathers are currently used to estimate subsurface velocities.

In the frequency domain, equations 6-4 and 6-5 have the forms in equations 6-6 and 6-7.

(6-6)
$$I(x,z,h) = \frac{\sum_{\omega} \overline{S(\omega, x-h, z)} P(\omega, x+h, z)}{\sum_{\omega} \overline{S(\omega, x-h, z)} S(\omega, x+h, z)}$$

(6-7)
$$I(x,z,h) = \frac{\sum_{\omega} \overline{e^{i\omega\tau} S(\omega, x, z)} P(\omega, x, z)}{\sum_{\omega} \overline{e^{i\omega\tau} S(\omega, x, z)} S(\omega, x, z)}.$$

Shot Profile Migration Example

The black lines in Figure 6-7(a) show the location of three shots with receivers spanning the entire model. Part (b) shows one-way shot profile migrations of these shots. Note that each migration images a substantial portion of the subsurface. These images were actually produced using the imaging condition of Equation 6-3. Thus, the process included approximate correction for illumination.

Figure 6-7. Shot profile images

(a). A Gulf of Mexico Earth model and synthetic shot profile

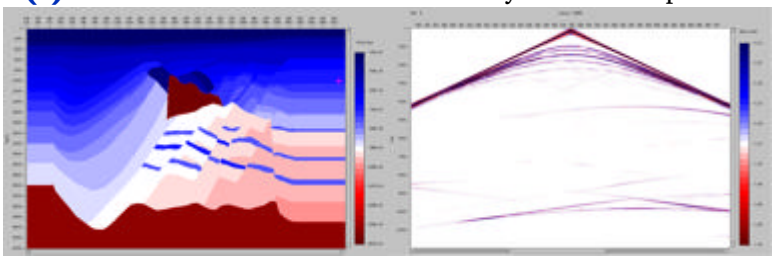

(b). Shot profile migrations of shots over the model in (a)

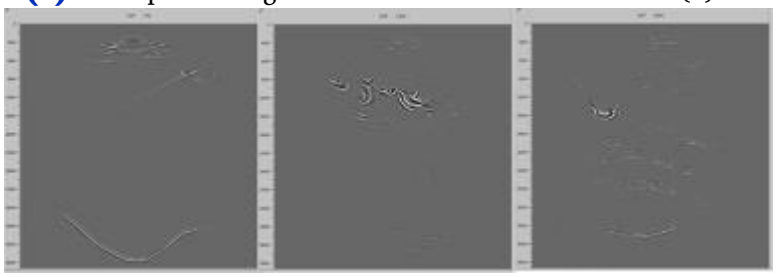

As noted earlier, every algorithm in Figure 4-1 can be used as part of a shot profile style migration method.

- Pure XT algorithms are either one-way or two-way and are usually implemented using finite difference approximations.
- Of the FK methods, only the PSPI method is popular.
- The most popular one-way method is based on the FKX phase screen method of Ru Shan Wu and colleagues, or on methods that are slight variants of this technique.
- Plane wave modeling techniques are also in demand because they can be applied very efficiently.
- In contrast, raytrace (Kirchhoff) shot-profile approaches are not popular because this method is usually implemented to image common-offset volumes rather than shots. This structure facilitates the production of common-offset image gathers, and their use directly affects estimation of interval velocities.

Combinations of these methods are rare. Some that probably should have received attention include combinations of Gaussian Beam and two-way-reverse-time, as well as Gaussian Beam and one-way-phase screen or PSPI.

Partial Prestack Migration: Azimuth Moveout (AMO)

Except for pure land acquisition, it is generally very difficult to record pure common offset or pure common azimuth data. Economics limits such recording on land, and cable feather makes marine acquisition of such data almost impossible. Consequently, methods have been developed to map recorded data into the proper framework. One such approach is *azimuth moveout* (AMO), which is the combination of DMO to a zero offset, followed by inverse DMO to a fixed non-zero offset. Figure 6-8 is a revision of Figure 3-30.

Figure 6-8. Constant velocity non-zero offset equal traveltime curve.

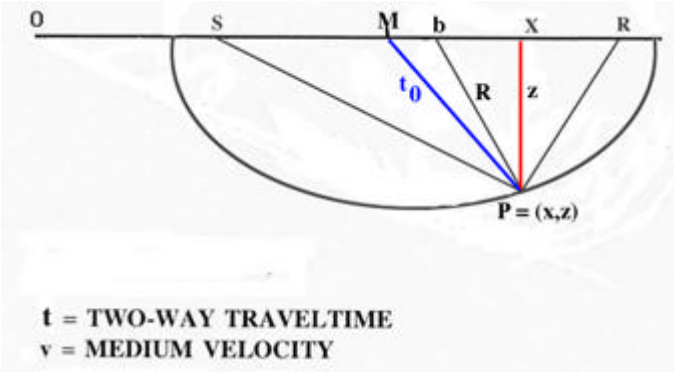

With a little bit of Greek mathematics, it shows that the time, t, of the equal traveltime curve in a constant velocity medium satisfies the elliptical equation in Equation 6-8, where, of course, t is the traveltime from S to P to R, and $h = (R - S)/2$ is the half offset.

(6-8)
$$\frac{x^2}{\frac{(vt)^2}{4}} + \frac{z^2}{\frac{(vt)^2}{4} - h^2} = 1$$

It is interesting to determine the time, t_0, in terms of v, t, and h, but doing so is not completely straightforward mathematically. What we first need to recognize is that t_0 in Equation 6-8 lies on the circle defined by Equation 6-9.

(6-9)
$$(x - b)^2 + z^2 = \frac{(vt)^2}{4}$$

For readers with a bit of calculus, if we take the derivatives of Equations 6-8 and 6-9 with respect to x, we get, respectively, Equation 6-10 and Equation 6-11.

(6-10)
$$\frac{x}{\frac{(vt)^2}{4}} + \frac{z\frac{\Delta z}{\Delta x}}{\frac{(vt)^2}{4} - h^2} = 0$$

(6-11)
$$(x - b) + z\frac{\Delta z}{\Delta x} = 0$$

Note that $\Delta z/\Delta x$ is the slope of the local tangent or, more practically, the slope of the reflecting migrated event if P was its location. Using Equation 6-11 to eliminate $\Delta z/\Delta x$ from Equation 6-10 yields Equation 6-12.

(6-12)
$$b = \left(1 - \frac{\frac{(vt)^2}{4} - h^2}{\frac{(vt)^2}{4}}\right) x$$

After simple algebraic manipulations, the result is Equation 6-13. What this formula tells us is that the zero-offset time, t_0, is a function of the offset, h, the velocity, v, and the traveltime, t.

(6-13)
$$t_0^2 = \left(t^2 - \frac{4h^2}{v^2}\right)\left(1 - \frac{b^2}{h^2}\right) = t^2\left(1 - \frac{b^2}{h^2}\right) - \frac{4h^2}{v^2}\left(1 - \frac{b^2}{h^2}\right)$$

A key point is that t is the input time on the input trace and t_0 is the zero-offset time. What we want a DMO process to do is to map data at time t to data at time t_0. A bit of trickery due to D. Forel and G.H.F. Gardner (1986) makes this possible. What they wanted after DMO processing was a data set that satisfied an equation of the form in Equation 6-14 for each *new* offset k.

(6-14)
$$t_1^2 = t_0^2 + \frac{4k^2}{v^2}$$

They realized that, given t_1 and k, they could rewrite Equation 6-13 in the form of Equation 6-15.

(6-15)
$$t_1^2 = t^2\left(1 - \frac{b^2}{h^2}\right) + \frac{4}{v^2}[k^2 - (h^2 - b^2)]$$

Then, if they chose $k^2 = h^2 - b^2$, the result would be Equation 6-16, which simplifies to Equation 6-17.

(6-16)
$$t_1^2 = t^2\frac{k^2}{h^2}$$

(6-17) $$t_1 = t\frac{k}{h}$$

Thus, all DMO amounts to is a simple mapping from offset h at time t to offset k at time t_1. Moreover, this mapping is entirely velocity independent. This means that DMO and, consequently, DMO inversion can both be performed in a completely velocity independent manner. Forel and Gardner also realized that this process can be carried out by replacing each input trace with an ensemble of output traces having offsets determined by k through b at time t_1.

Figure 6-9(a) shows an ensemble of replacement traces for DMO on the left and DMO inverse on the right. As we might expect, what we see are smiles for the former and frowns for the latter. Figure 6-9(b) shows what happens to a purely inline common-midpoint gather after DMO is applied. Note that, after DMO, the source-receiver axis is orthogonal to the input source receiver axis. If we apply DMO inverse to the DMO'd data, the result would be to simply rotate back to the original orientation.

Figure 6-9. DMO in pieces

(a). DMO impulse response on the left and DMO inverse on the right

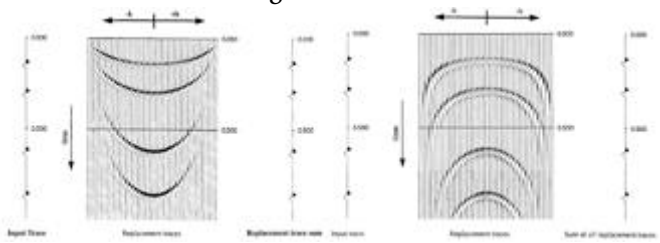

(b). DMO is essentially a 90 degree rotation

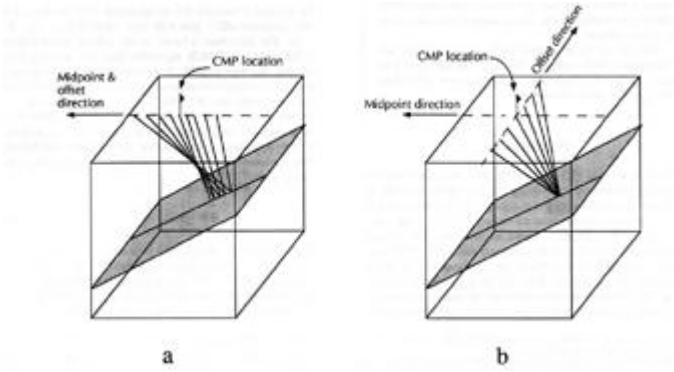

Figure 6-10 shows how to modify AMO (DMO followed by DMO inverse) to achieve an output source-receiver orientation of any desired angle. DMO is first applied along the output trace orientation indicated by the h_O vector in part (b). DMO inversion is then applied orthogonally to this direction. This process transforms an input volume with virtually random azimuths into one with a fixed azimuth and only four dimensions.

Figure 6-10. Arbitrary angle AMO

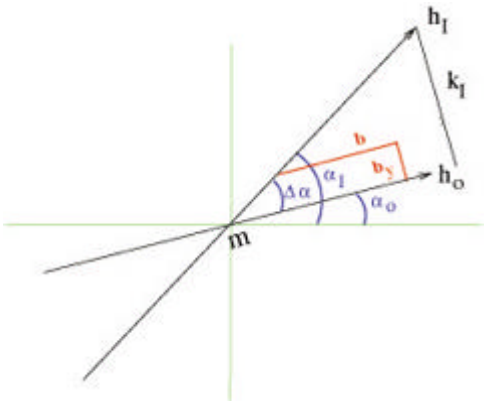

Figure 6-11 shows an AMO impulse response on the left and a full 3D volume on the right. The input trace from the SEG/EAGE C3-NA synthetic data volume used for the impulse response had an azimuth of -2 degrees and an offset of 1600 meters. All traces from the SEG/EAGE C3-NA data were used to produce the 1000 meter offset volume on the right. The azimuth of this volume was 45 degrees.

Figure 6-11. AMO impulse and 45 degree azimuth at 1000m offset.

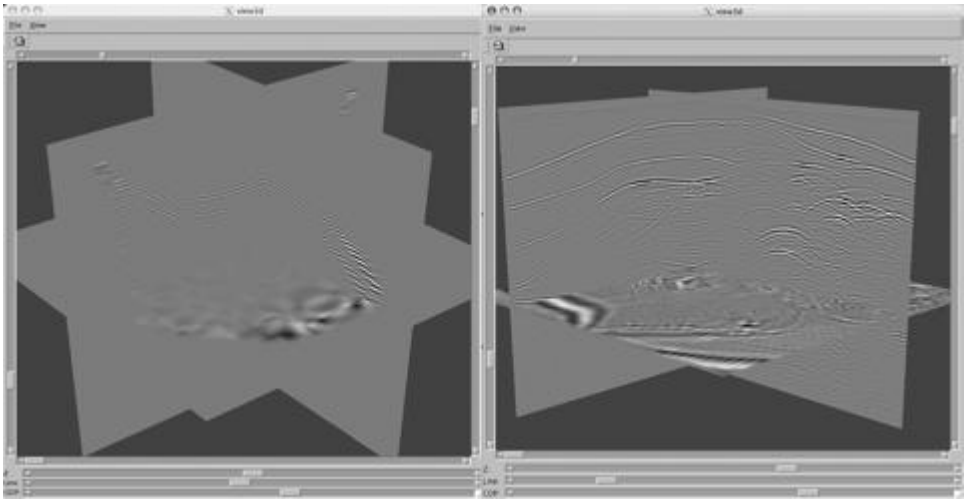

The left hand side of Figure 6-12 shows a 1000 meter offset slice through an AMO'd volume processed to achieve zero degrees azimuth. The right hand side shows the same line from a similarly processed volume at 45 degrees. Note the considerable differences in reflector position even though the model is the same.

Figure 6-12. A comparison of zero degree and 45 degree azimuths.

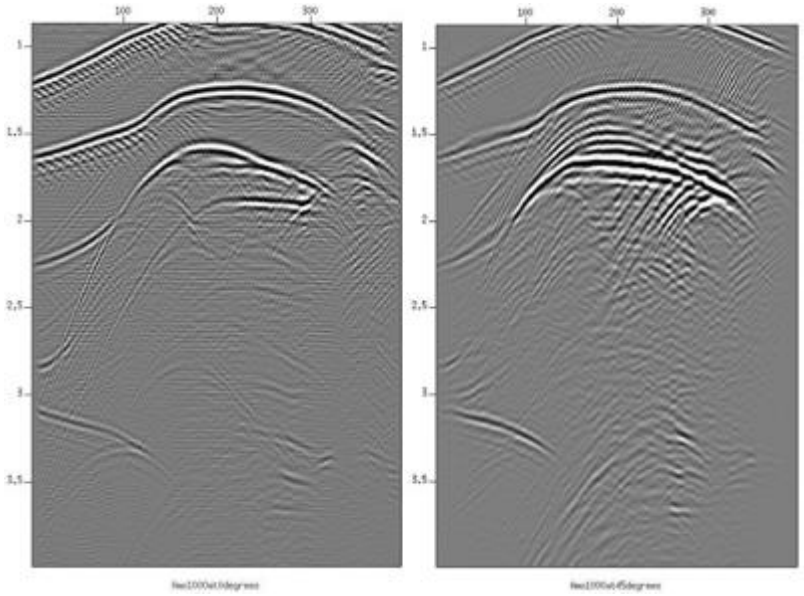

The top half of Figure 6-13 shows a fixed 15 degree azimuth line selected from a single streamer marine acquisition from offshore Indonesia. Shots with mostly shorter offsets are on the left, while those with mostly longer offsets are on the right. The bottom part of this figure shows a selected set of shots from the 3D AMO processed data set. Note the similarity of these data as well as that all offsets are now present in the common azimuth line.

Figure 6-13. Real data AMO example

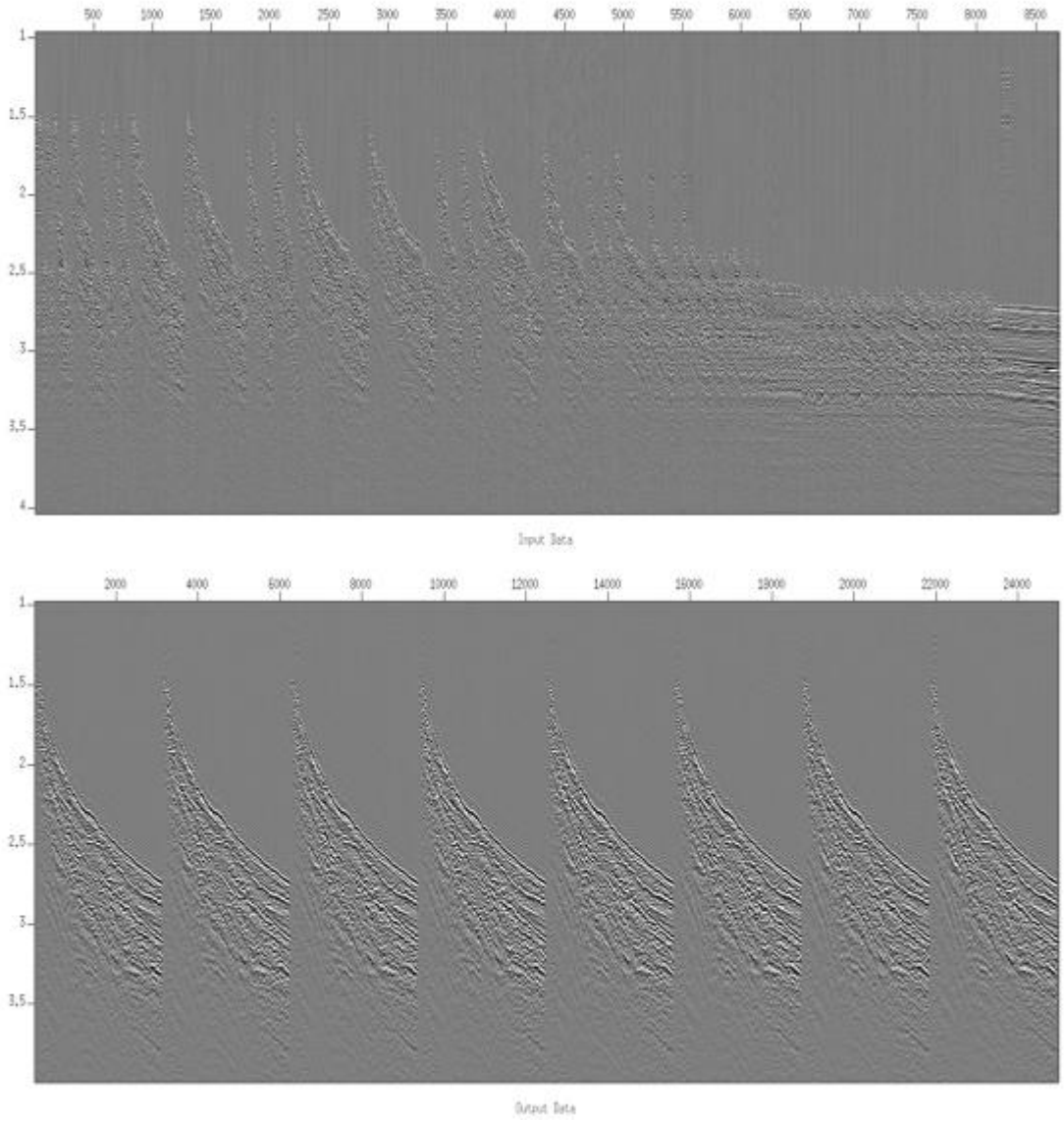

Velocity Independent Prestack Time Imaging

Figure 6-14 shows various slices through the seismic response for a point reflector in a purely constant velocity medium. The top left figure is the response due to a single point reflector. Proceeding in a counterclockwise manner, we see a common-depth point slice, a radial or common-angle slice, a common-time-slice, and finally in the upper right, a common offset slice. In this constant velocity world, it should not be difficult to envision a method for imaging each of these particular orientations of the data.

Figure 6-14. Point response in a constant velocity medium

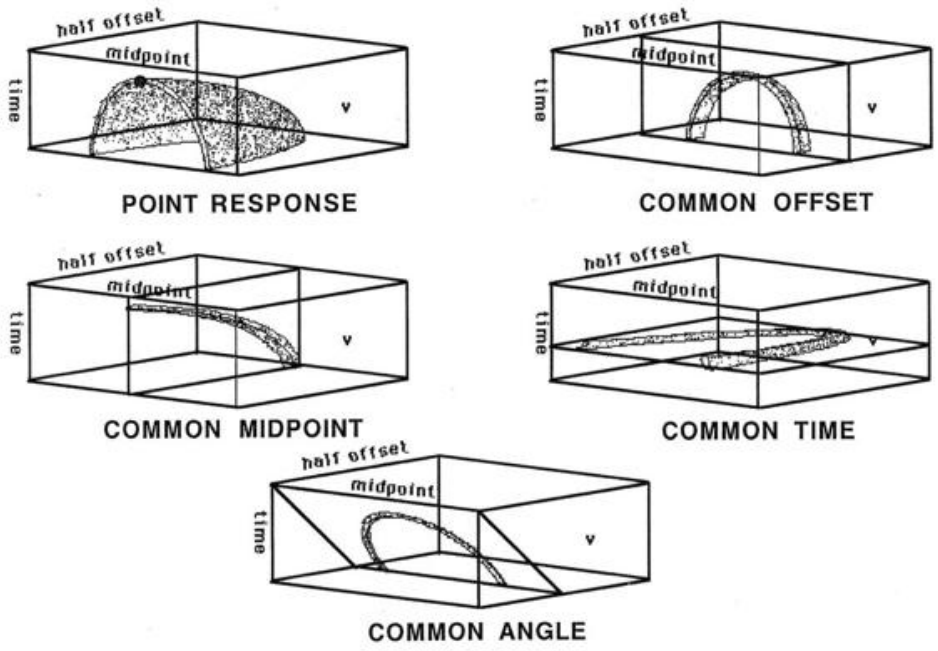

Common-offset sections actually look like normal stacked seismic sections, but there is a difference. In the near offset on the left side of Figure 6-15, the section closely resembles a normal stack, while the far offset on the right appears to be a squeezed version of the section on the right. Even though these sections are from the two dimensional anisotropic model in the lower right hand corner, anisotropy is not really visible to the naked eye. Moreover, traditional normal moveout correction, even though it supposedly stretches the data to equivalent zero-offset time, will not ultimately produce anything close to a true zero-offset stack.

Figure 6-15. Near and far offsets

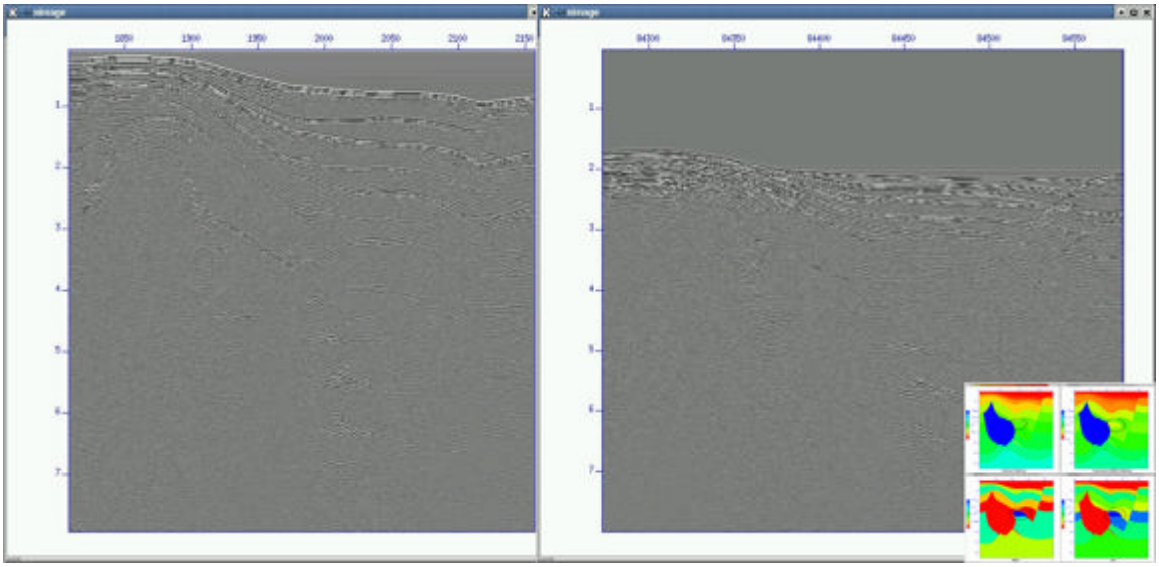

Figure 6-16 details an unusual methodology for imaging or migrating data in constant velocity media. It combines what we have learned in the previous figures to allow us to image the point source response while delaying the velocity analysis until the very end.

Figure 6-16. Dip independent prestack imaging

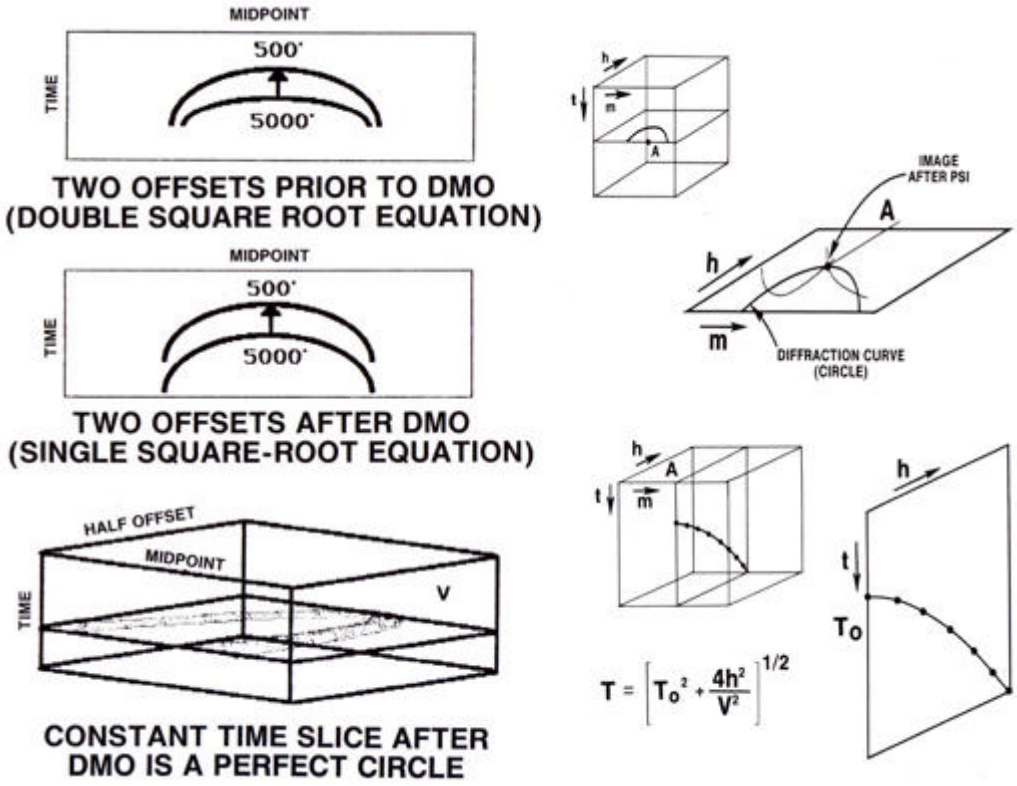

The left hand side of this image essentially shows what happens when we apply DMO. The top graphic shows the input data from a single point source. That is, it represents two different common-offset slices superimposed on one another. The middle figure on the left hand side shows the same two offset slices after DMO. Note that, in this case, the two common-offset images differ only by moveout time.

In the bottom part of the left hand side, we see that, after DMO, any time slice appears to be a circle. That being the case, we can image this circle to a point by simply migrating it as in the previous figures. Once this is done, as indicated by the top figure on the right, we will have reduced the point source response to a single CDP whose moveout velocity provides the necessary information to image the point at its correct subsurface location.

The completely velocity independent prestack imaging method that produced Figure 6-17 delayed velocity analysis until the very end of the process. This means that the velocities obtained from this approach are actually migrated velocities, and consequently are measured almost vertically. The importance of this statement is that this set of velocities are much more consistent with the assumptions made to ensure the accuracy of the traditional Dix vertical inversion scheme.

Figure 6-17. Application of dip independent prestack imaging in the Gulf of Mexico

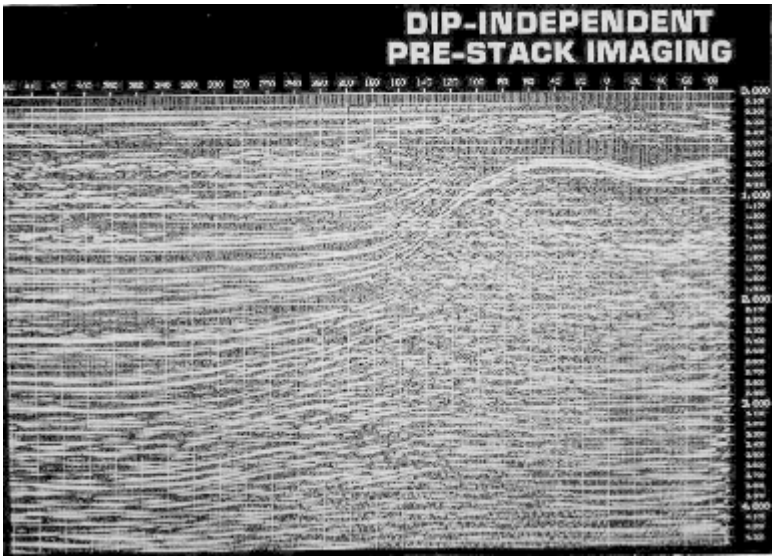

Double Downward Continuation—Common Azimuth Migration

Among the several approaches to prestack imaging, common azimuth migration is one of the fastest. While it may suffer from off-azimuth response problems, it produces usable output at a speed that makes it a viable technique for velocity analysis and velocity model construction.

Figure 6-18 shows a common azimuth migration. A common azimuth migration parameterizes input data by CDP and offset. Since the data are assumed to have been recorded with one and only one azimuth, the source and receiver locations can be computed from the midpoint (or CDP) and offset. This means that the data are defined by only four parameters: midpoint (2), offset (1), and time, and, as a consequence, are four-dimensional. Normally, data sets with more than one azimuth are really five-dimensional: source(2), receiver(2) and time (1).

Figure 6-18. Common azimuth downward continuation migration

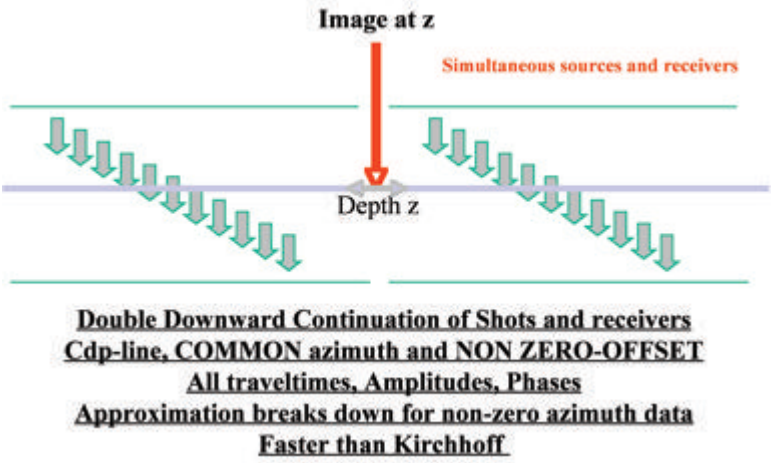

The nice thing about common azimuth data is that they can be continued downward in the same manner as poststack data. Even though the poststack data set has only three-dimensions, the methodology of the two approaches is so similar that we can certainly think of them as being the same.

The disadvantage of the common azimuth approach is that real world data is never acquired in common azimuth form. Moreover, the approximations used to produce the algorithm usually result in a methodology that cannot image steeply dipping events well.

Perhaps the saving grace of this algorithm lies in its speed. For full volume migrations, it has the potential to be the fastest algorithm ever invented for prestack imaging.

Again, as was the case for poststack data, common azimuth approaches image the data one depth slice at a time. Figure 6-19 is just an illustration to emphasize that almost all one-way methods image the data one depth or time slice at at time.

Figure 6-19. Common azimuth depth slice from a migration of the SEG/EAGE C3-NA data set

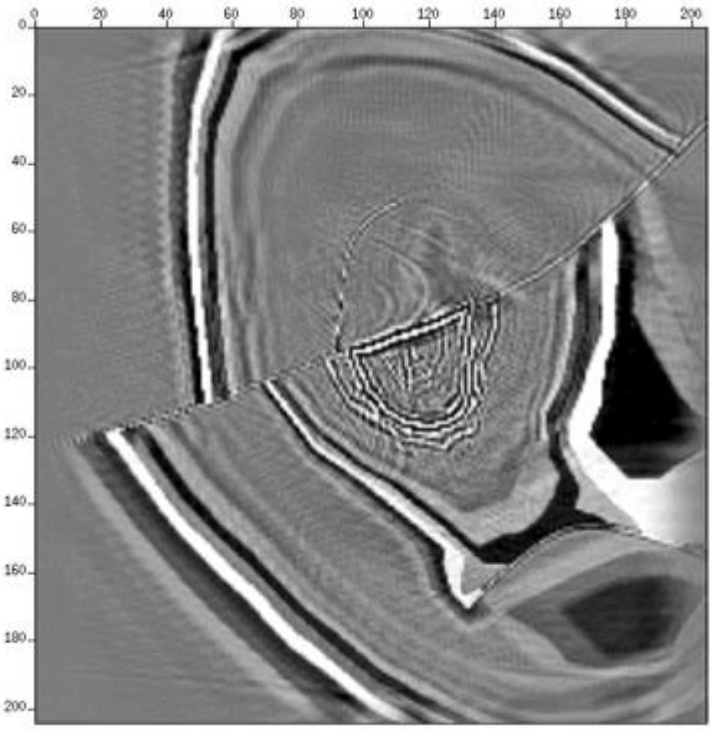

The nice thing about common azimuth migration is that it reduces the complexity of the input data set by one dimension. Normal 2D data is actually three-dimensional—it is indexed by one space variable for the shot location, one for the receiver, and one for time. In contrast, 3D data is characterized by being five dimensional, where each shot location has at least two surface coordinates, each receiver also has two surface coordinates, and, of course, there is one time dimension. Since shot, $m + h/2$, and receiver locations, $m - h/2$, are a simple function of the midpoint coordinate vector, m, common azimuth data has four dimensions, with two midpoint coordinates, one offset, and time. As a result, downward continuation of data of this type is much simpler that downward continuation of more typical five-dimensional 3D data sets.

However, common azimuth processes are not without problems. For example, the approximations necessary to make the methodology efficient are known to break down at 45 degrees. Furthermore, dip limits can be severe if the implementation does not properly account for different velocities at source and receiver coordinates. Nevertheless, for a large percentage of the subsurface, common azimuth migration is a useful, efficient tool for velocity model construction on a densely-spaced grid.

Aliasing is as much of an issue for common azimuth migration as it is for almost any other type of wave-equation based method. Whether data is recorded at good or bad spatial increments, aliasing must be considered and handled. For example, if it is based on the formulas above, the acquisition *dx*, *dy* and desired *dz* do not support a maximum frequency consistent with the recording parameters, the output spacing can be adjusted so that these frequencies will be imaged without aliasing. Normally, this consideration is not an issue with Kirchhoff-based technologies, since implementations of this type usually handle aliasing correctly without much user consideration. Because it is a recursive process, one-way downward continuation must be performed so that the output spacing precludes any aliasing at every depth step. This is particularly true at the initial downward propagation, but must be maintained until the recorded frequency has dropped below the point where the surface acquisition increments are satisfactory.

In addition to requiring proper spatial increments, common azimuth approaches require input data that is properly sampled in offset. The input offset increment must be chosen to ensure that offset dependent arrivals are not aliased.

Common Offset Kirchhoff Ray-Based Methods

Kirchhoff migrations have long been a staple of imaging technology. As a result, there are many excellent implementations of this methodology. Almost all are so-called single arrival approaches, whether in time or depth. Generally speaking, when the velocity gradients are reasonable, single arrival methods have excellent capabilities and can produce excellent images. On the other hand, when overburden velocity variations are strong, Kirchhoff methods can have significant problems imaging below these variations.

Straight Ray Kirchhoff Prestack Time Migration

The process described in Figure 6-20 provides the basic schema for all single arrival prestack Kirchhoff time and depth migrations.

Figure 6-20. Straight ray prestack Kirchhoff time migration.

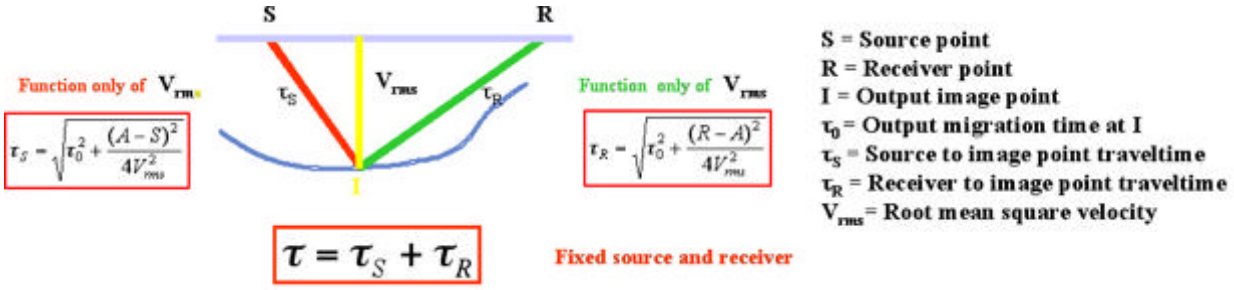

The process gives a simple velocity dependent recipe for computing a source to image-point traveltime and an image-point to receiver traveltime for use in the migration. In this prestack case, a closed form local RMS velocity formula produces the required times. The sum of these two traveltimes is then used to select an amplitude from the trace with this source and receiver. We then calculate a correction amplitude for this image point, multiply it times the amplitude selected from the trace, and add the result to the output image location. To avoid aliasing, it is normal to filter the trace using the usual aliasing equation in Equation 6-18.

(6-18)
$$f_{max} = \frac{v_{min}}{4\,dx\cos\theta}$$

Equation 6-18 is used to compute a dip dependent upper frequency to restrict the frequency content of the trace prior to adding the extracted amplitude into the corresponding output image point. The simplest version of this type of anti-aliasing pre-computes several traces with decreasing frequency bands and then selects the desired amplitude from the one most likely to avoid aliasing issues.

Curved Ray Kirchhoff Prestack Time Migration

The curved ray Kirchhoff prestack time migration algorithm shown in Figure 6-21 is based solely on the curved ray formulas in Figure 4-19. Those formulas are used to compute source to image point and image point to receiver traveltimes. Typically, the required $v(z)$ velocity is selected at the image point, but it is clearly possible to select one at the source and a different one at the receiver.

Figure 6-21. Curved-ray-prestack-time-Kirchhoff migration.

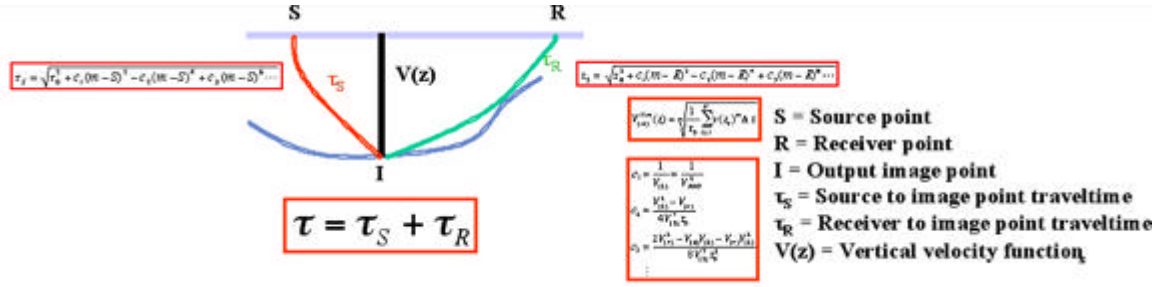

Single Arrival Kirchhoff Depth Migration

As indicated in Figure 6-22, the only difference between various Kirchhoff prestack time migrations and Kirchhoff depth migrations lies in how the required traveltimes are computed.

Figure 6-22. Single-arrival-Kirchhoff-depth migraiton

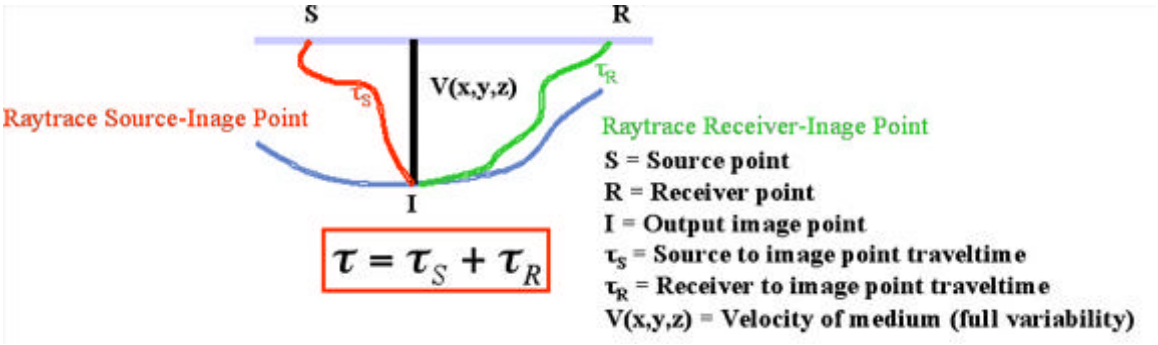

Raytracing is by far the dominant method for calculating these traveltimes. In this figure, rays are traced from the source and the receiver to the output image point. The traveltime sum, along with appropriate amplitude corrections, is then used to sum the trace amplitude into the output image point. On the surface, this process requires that rays be traced from each source and receiver to each output image point. Computing a traveltime volume for each and every source and receiver location can be very expensive, so as shown in Figure 6-23, most modern Kirchhoff implementations precompute traveltimes on a regular grid.

Figure 6-23. Raytracing issues for all 3D raytrace based imaging methods

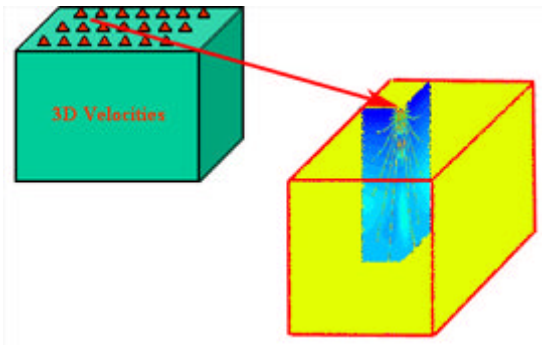

It is possible that more than one ray will arrive at any given image point during the calculation. Since keeping track of every such arrival is an extremely complex bookkeeping problem, it usually easier to choose a single arrival, but the selection of the arrival best serving the migration process is not always easy. Typical arrivals of this type are maximum energy, minimum distance, or minimum velocity.

Minimum velocity arrivals avoid headwaves caused by proximity to salt or other high velocity structures. Thus, in areas with strong lateral velocity variations, such as salt regimes, the minimum velocity methodology is considered to be optimum. In such cases, the minimum velocity ray is defined to be that ray for which the sum of all velocities along the ray has the smallest value. Interpolation is used to compute the desired traveltime at each source, receiver, and image point, thus reducing the overall computation costs and generally improving the speed of the migration step.

Clearly, the accuracy of the migration is controlled by how well the implementation handles both the traveltime computations and the interpolation of the traveltime volumes.

Multiple Arrival Kirchhoff Migration

Energy from a seismic source can reach any given subsurface point in more than one way. Figure 6-24 characterizes this concept graphically in terms of rays. Each ray is uniquely determined by either its take-off angle or by its arrival (incidence) angle, and there is no restriction on how many rays from a fixed source location can reach any given subsurface point. To properly implement an algorithm of this type we must, at least in theory, calculate an amplitude and a phase-shift for each arrival to correct the selected amplitude from the current input trace.

Figure 6-24. Multiple-arrival-prestack-Kirchhoff-depth migration

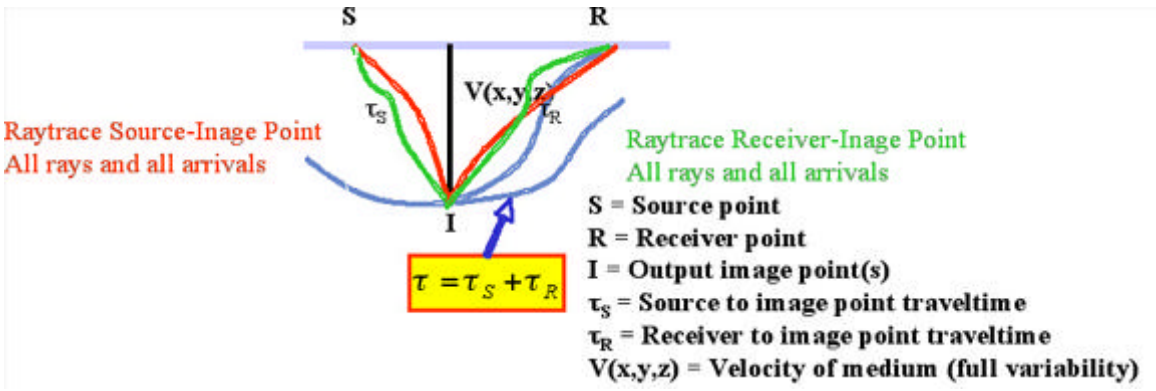

Multi-arrival Kirchhoff migration is very difficult to implement since it presents a rather complex bookkeeping problem that apparently has no efficient solution. This is unfortunate because multi-arrival Kirchhoff migration has the greatest potential for providing an algorithm with a near optimum percentage of the features of full two-way imaging. Based on empirical observations from the myriad implementations of its single-arrival brother, it would have super dip response, excellent amplitude handling, as well as the ability to include turning rays and diffractions.

Kirchhoff Elastic Depth Migration

The separation between acoustic and elastic Kirchhoff migration algorithms is solely determined by traveltime calculations. The migration step is not dependent on how the traveltime volumes are computed. If the traveltime volumes are based on acoustic equations, the result is an acoustic migration. If they are based on anisotropic calculations, the result is an anisotropic migration. If the source traveltimes are based on compressional velocities and the receiver traveltimes are based on shear velocities, the resulting algorithm is a converted wave migration.

Single Arrival Kirchhoff Depth Migration Summary

As the current work-horse of seismic depth migration and migration velocity analysis, single arrival Kirchhoff migration has proven to have excellent dip response, good amplitude response, and has shown some ability to image turning ray energy. Its great flexibility as a velocity analysis tool suggests that it will be around for some time to come. Its single biggest drawback is that it is very sensitive to strong lateral velocity variations, particularly below salt structures. This is very likely due to the use of a single arrival.

Raytrace-based migrations rely heavily on the quality and accuracy of their traveltime generators. As a high-frequency approximation to forward wave-field propagation, raytracing can be very sensitive to even relatively minor velocity variations. Reducing this sensitivity usually means that the input velocity field must be smoothed before calculating traveltime tables. In some cases, this is not an issue, but when the velocity variation is strong, significant depth errors may result. The raytrace module must compute both the traveltime to a given image point and any and all amplitude correction factors. If the raytracer is inaccurate, so is the output image, and no raytracer can recover from an incorrect velocity field. Likewise, no velocity field can be recovered from an incorrect raytracer.

When using Kirchhoff style methods, it is extremely important to understand how, when and where traveltime volumes are computed. If the migration algorithm is based only on downward, single arrival raytracing, then each volume must be sampled sufficiently well in all directions to ensure proper accuracy. In some Kirchhoff implementations, traveltime generators are based on finite difference solutions to the basic Eikonal equation that governs ray propagation. Because Eikonal-based methods are generally only able to calculate first arrivals, they are prone to producing spurious results in complex geological models.

Raytrace methods facilitate the calculation of multiple arrivals, and the selection of the most appropriate arrival better serves the migration process. Raytracing is the preferred traveltime generation method.

The utilization of a single arrival in Kirchhoff depth migration technology is one of the chief reasons these methods have difficulty imaging below complex structures. When we use all of the possible arrivals, as shown in Figure 6-24, we can achieve a superior result to what is achieved with the single arrival approach. While multiple arrivals complicate the migration algorithm and generally make it more computationally costly, the benefit of including more arrivals usually outweighs the increased cost. However, because it is so difficult to solve the general bookkeeping problem involved in making a multi-arrival Kirchhoff practical, this approach is seldom used.

Beam and Plane Wave Migrations

Beam and plane wave migrations can be divided into the following cases:

- pure plane wave
- beam stack
- delayed shot
- Gaussian beam

Pure Plane Wave Migration

The migration algorithms in the previous section are all based on downward continuation concepts. Conceptually, each such approach either uses the reversed wavefield as a source term and models the response in reverse, or it uses the reversed wavefield to downward continue the recorded data and produce an image at each depth slice.

The next two algorithms are based on concepts that use surface emergence angles to develop algorithms that produce similar images although they use widely different techniques.

We can also do the decomposition on common-offset sections shown in Figure 6-25. This is similar to slant stacking a stack. In this case, the section is a synthetic at 1000 meters offset, but for all intents and purposes, it looks just like a stacked section. Note that the short black dip element carries the sum of the information necessary to figure out its final position (the red dip element). A two-point raytracer can figure this out quite easily.

Figure 6-25. Fixed offset hand migration

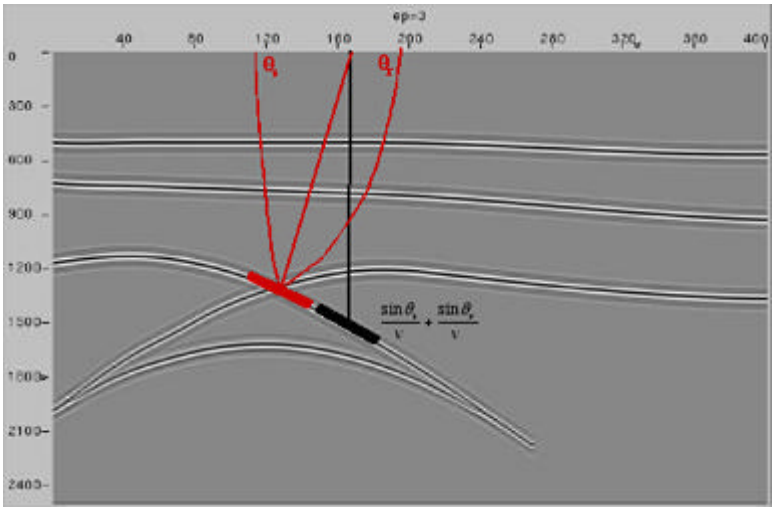

Figure 6-26 illustrates the process for one of the fastest migrations possible. Given the local dip information from the previous figure, a two-point raytracer gives us the position of the dip element. All we need is a bit of the local wavelet to place at the center of the image zone rectangle.

Figure 6-26. Ultra fast beam migration

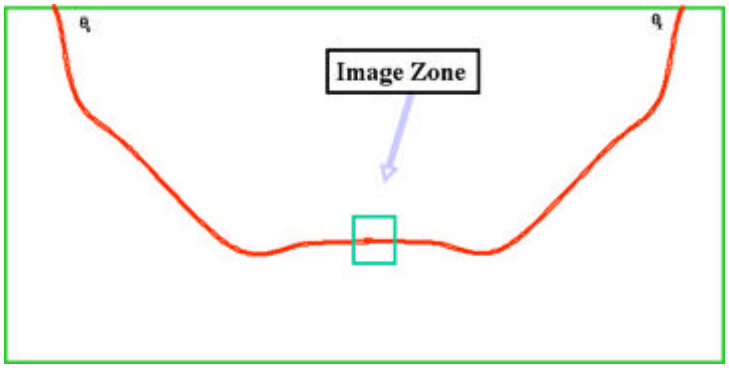

Beam Stack Migration

We get a bit more than just the emergence angles when we find the local dip element shown in Figure 6-27. In this case, the local dip is the sum of the source traveltime gradient and the receiver gradients. Since we know these two values when we calculate the traveltimes, we can construct another beam style migration element through a diffraction stack.

Figure 6-27. Using local dip estimates

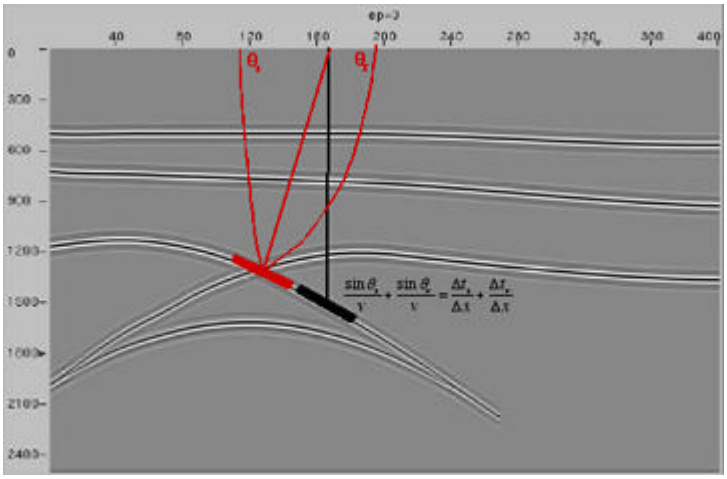

Converting a Kirchhoff method to a beam or slant stack approach requires that we expand traveltime around a central source (or receiver) location in a Taylor series. In two-dimensions, the proper formula is given by Equation 6-19.

(6-19) $$\tau_0 + p_{x_s} \bullet (x = x_s)$$

Here, p_{x_s} actually turns out to be the derivative (gradient in 3D) of the traveltime with respect to source position; that is,

(6-20) $$p_{x_s} = \frac{\Delta\tau_s}{\Delta x_s}$$

Since p_{x_s} can be calculated during the raytracing part of the Kirchhoff method, there is little added computational cost. On the other hand, since the entire slant stack bundle replaces many traces in the migration process, Kirchhoff-beam-stack methods can be significantly more efficient than their traditional straight-forward implementations.

Figure 6-28. Generalized Traveltimes and Beam-Stack Kirchhoff Migration

(a). Computing traveltimes from centered traveltimes

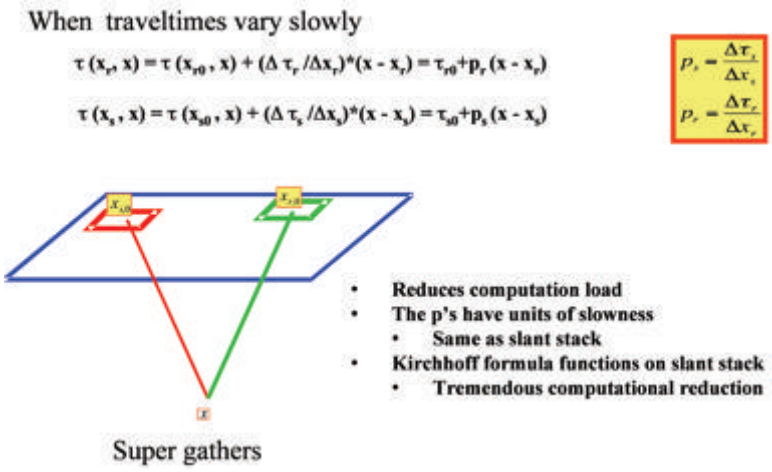

(b). Schematic of a traveltime bundle

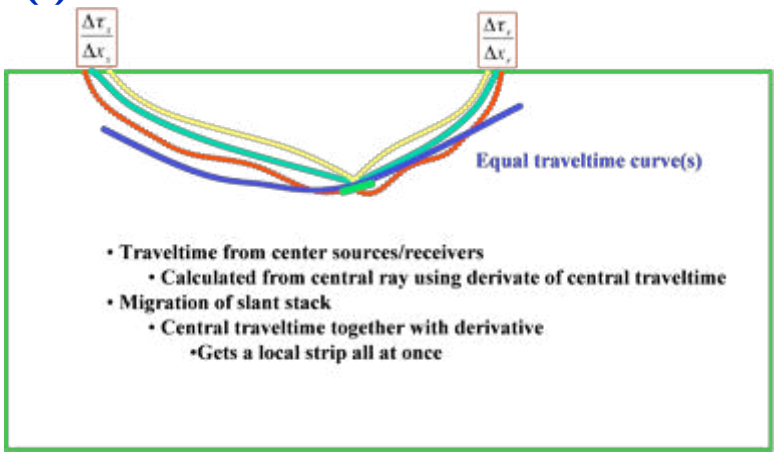

Delayed Shot Migration

Figure 6-29 illustrates the basic concepts underlying plane-wave or common-emergence angle calculations for source and receiver gather plane wave decomposition. The first step is to decompose the data into plane wave sections. In the case of a synthetic source, we simply decompose the source along the normal to the p value. For receiver gathers, holding p fixed produces a p gather or p-section. Such sections are obtained through a simple slant stack of the data around some central point. To propagate a source, we simply do the propagation along the common angle. To back propagate a receiver decomposition, we simply back-propagate each p. Depending on which algorithm we choose, each common p-section can be migrated individually. After migration, we only need to sum the results to produce a final migrated result.

Figure 6-29. Delayed shot and receiver migration

(a). Delaying shots or receivers to synthesize a plane wave source

(b). Shot and receiver delay migration principles

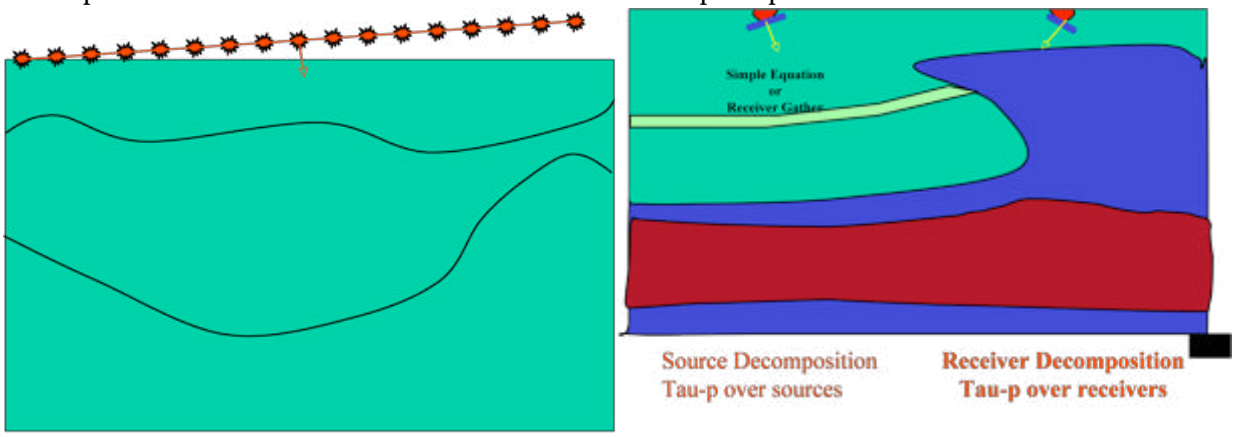

Figure 6-30 illustrates that each p-value in the slant stack produces a common emergence section that can be migrated in much the same manner as a common-offset stack, or even, conceptually, a zero-offset stack.

Figure 6-30. A common p section

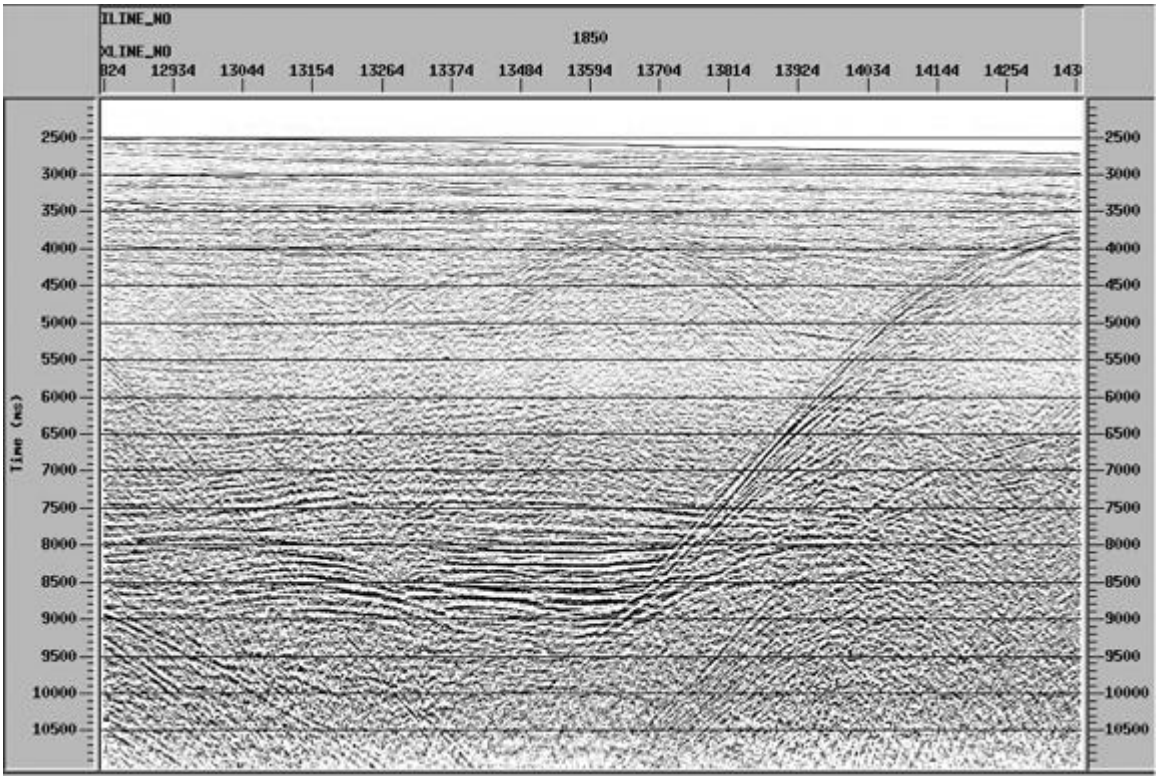

The utilization of slant-stacked data has many advantages and many draw-backs. An important drawback is the need to use a large number of p-values to adequately cover the entire impulse or operator response. Typically, theory requires us to use hundreds of such values, but most implementations are efficient only if the process uses a few values.

Gaussian Beam Migration

Figure 6-31(a) shows how a forward propagated shot can be constructed through the use of what are called Gaussian beams. Computation of each such beam requires that we first shoot a central ray. The velocity function, $v(s)$, selected along the ray path is then used to propagate source energy forward along this ray. We can use almost any kind of propagator for this process, but usually something like a phase shift is the algorithm of choice. During the back-propagation, energy is allowed to expand from the central ray, and is controlled predominantly by a Gaussian bell-style weight, with the local size depending on the propagation distance and local sound speeds. Because each central ray is defined by its take-off angle, and each such angle is in turn a plane wave direction, we can say that Gaussian beam modeling is really a plane wave modeler.

Figure 6-31. Shot modeling and prestack migration via Gaussian beams

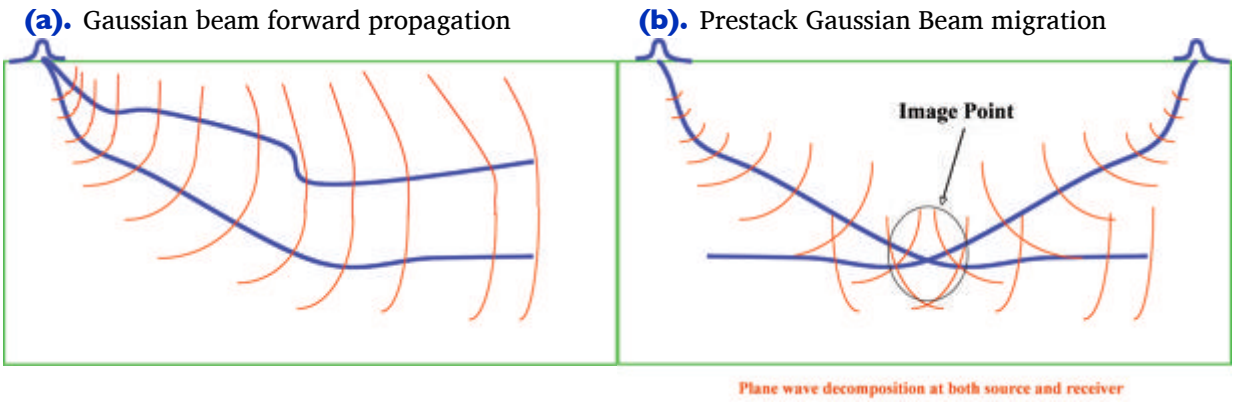

Figure 6-31(b) shows how to use the concepts discussed in part (a) to construct a Gaussian beam approach to prestack migration. Note that Gaussian weighting is applied to each p-value in the slant stack of a bundle of local traces.

Gaussian beam migration has many positives, including that it does not suffer from the single arrival problems associated with traditional Kirchhoff migrations, and it can be implemented in a manner that correctly handles amplitudes and even multiple arrivals. Consequently, Gaussian beam methodologies tend to produce images that are extremely close to full-wave equation methods. In fact, they are much closer to two-way methods than one-way approximations to the wave equation.

Algorithmic Differences

Figure 6-32 shows the basic differences between different migration algorithm classes.

Figure 6-32. Prestack migration differences

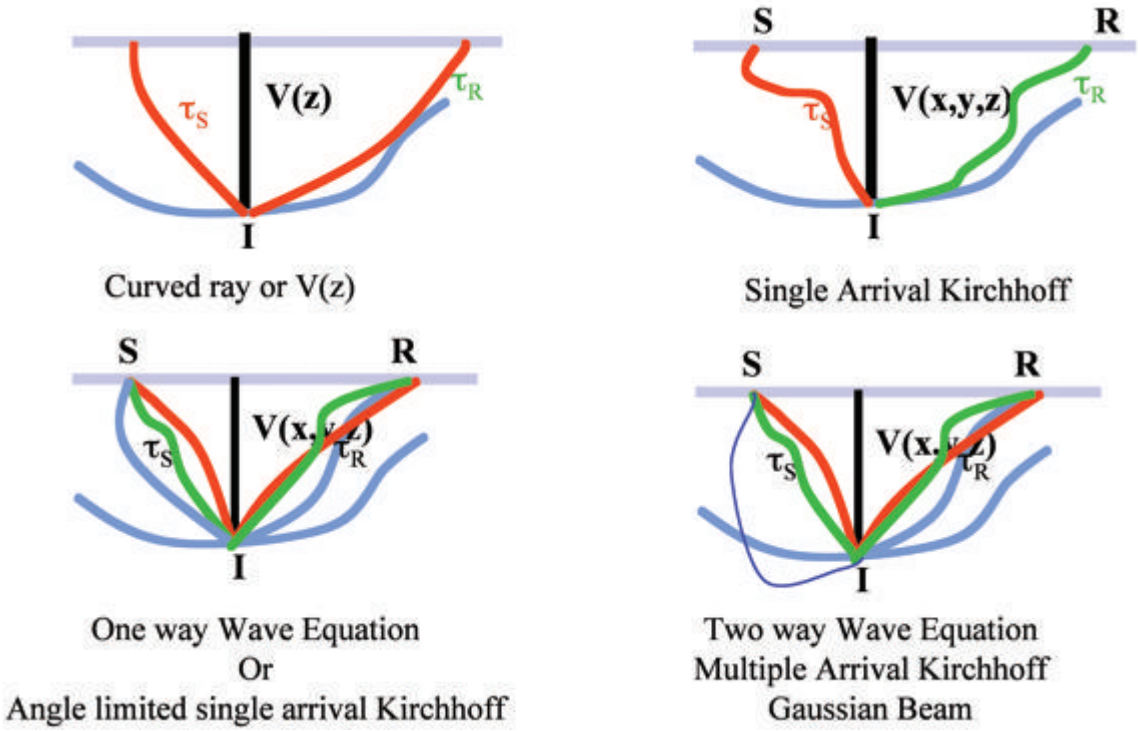

The top left part of the figure is a schematic of a typical curved-ray time migration. Note that this approach uses a single arrival and also uses a single $v(z)$ velocity for each output image point. This means is that the curved ray time migration is really a $v(z)$ depth migration that uses a completely different model for each and every output point.

The top right part of Figure 6-32 conceptualizes a single arrival Kirchhoff depth migration. Here, the single arrival is chosen by shooting rays in a fully three-dimensional Earth model. In this case, the migration is a truly three-dimensional process. In complex media, the forced choice of a single arrival increases this method's sensitivity to rapid and strong velocity variation. It is not surprising that single arrival Kirchhoff depth migration has considerable difficulty imaging below salt structures. Nevertheless, the flexibility of this approach means that it will remain the workhorse of migration velocity analysis for Earth model estimation.

The bottom left part of the figure shows a characteristic multiple arrival migration methodology. Among the techniques that achieve this goal are one-way FKX wave-equation algorithms and multi-arrival Kirchhoff methods that do not allow turning rays. Because turning rays have been eliminated, the methods envisioned in this figure cannot image beyond 90 degrees.

The bottom right part of Figure 6-32 illustrates a full, or at least nearly full, two-way methodology. In this setting, waves described by all incidence and reflections angles are imaged. The methods that have this kind of capability include full multiple-arrival Kirchhoff algorithms, Gaussian beam methods, and, of course, full finite difference reverse time migration.

To further understand migration differences, Figure 6-33 shows impulse responses from two different algorithms at three different trace locations in the velocity model. The vertical black lines mark the position of synthetic traces from the data set generated over the model. The top row of impulse responses are based on one-way FKX algorithms while the bottom row are based on a single arrival Kirchhoff method.

Figure 6-33. Comparison of impulse responses from a complex salt structure model

(a). Velocity Model **(b).** Impulse Responses

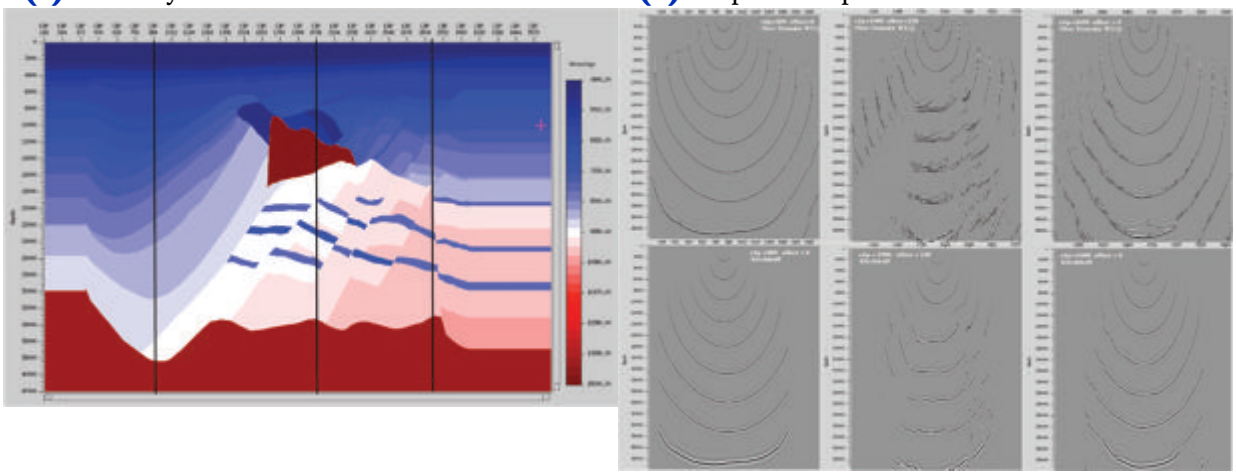

Because the left hand impulse response column represents a trace from that side of the model, the lack of strong lateral velocity variation results in almost identical wave-equation and Kirchhoff responses.

In contrast, the middle column represents a trace with a midpoint directly over the salt structure in the center of the model. Note that while the Kirchhoff amplitudes are comparable to those of the response in the top row, the tremendous number of multiple arrivals and phase changes are quite evident. It is possible to program the Kirchhoff response to almost exactly match the wave-equation response, but the effect is difficult to achieve.

Since the trace used to compute the right hand column is also out of the strong lateral velocity zone, its affect on arrivals is not as noticeable as the center column. Nevertheless, the need to compute a large number of multiple arrivals is still quite clear.

Figure 6-34 shows the extremely complicated impulse of both the two-way and one-way methods, and demonstrates the need to use highly accurate algorithms in complex

geological media. Many people would argue that the smooth structure of the Kirchhoff impulse response on the right is the correct approach. However, the best results are produced using the full two-way method on the left. In some cases, the most pleasing image to the eye is not the best approach to producing a full image.

Figure 6-34. A simple comparison of Kirchhoff, one-way and two-way impulse responses over the SEG/EAGE AA′ data set.